



Artificial neural networks for neutron/ γ discrimination in the neutron detectors of NEDA

X. Fabian^a, G. Baulieu^a, L. Ducroux^a, O. Stézowski^{a,*}, A. Boujrad^b, E. Clément^b, S. Coudert^b, G. de France^b, N. Erduran^c, S. Ertürk^d, V. González^e, G. Jaworski^f, J. Nyberg^g, D. Ralet^b, E. Sanchis^e, R. Wadsworth^h

^a Univ Lyon, Univ Claude Bernard Lyon 1, CNRS/IN2P3, IP2I Lyon, UMR 5822, F-69622, Villeurbanne, France

^b Grand Accélérateur National d'Ions Lourds – GANIL, CEA/DRF and CNRS/IN2P3, BP 55027, F-14076, CAEN Cedex 05, France

^c Faculty of Engineering and Natural Sciences, Istanbul Sabahattin Zaim University, 34303, Istanbul, Turkey

^d Department of Physics, Nigde Omer Halisdemir University, 51200 Nigde, Turkey

^e Departamento de Ingeniería Electrónica, Universitat de Valencia, Burjassot, Valencia, Spain

^f Heavy Ion Laboratory, University of Warsaw, Warsaw, Poland

^g Department of Physics and Astronomy, Uppsala University, SE-75120 Uppsala, Sweden

^h Department of Physics, University of York, Heslington, York, YO10 5DD, UK

ARTICLE INFO

Keywords:

γ -ray spectroscopy
Neutron detector
 n - γ discrimination
Pulse-shape discrimination
Machine learning
Artificial neural networks

ABSTRACT

Three different Artificial Neural Network architectures have been applied to perform neutron/ γ discrimination in NEDA based on waveform and time-of-flight information. Using the coincident γ -rays from AGATA, we have been able to measure and compare on real data the performances of the Artificial Neural Networks as classifiers. While the general performances are quite similar for the data set we used, differences, in particular related to the computing times, have been highlighted. One of the Artificial Neural Network architecture has also been found more robust to time misalignment of the waveforms. Such a feature is of great interest for online processing of waveforms.

1. Introduction

The NEutron Detector Array (NEDA) [1,2] is a neutron detector designed to be used with high resolution γ -ray spectrometers such as the Advanced GAMMA Tracking Array (AGATA) [3]. The liquid scintillator used in NEDA [4] is not only sensitive to neutrons but also to γ -rays. Since NEDA is being used as a neutron multiplicity filter, it is imperative to differentiate the interactions due to neutrons from those due to γ -rays. Because the excited molecular states (with decay constants 3.16, 32.3 and 270 ns) are being populated with different relative intensities for both particles, Pulse Shape Discrimination (PSD) techniques can be applied to distinguish them. Some traditional methods, i.e. the charge comparison [5,6] or the integrated rise time [7,8], have been implemented in analogue electronic modules for a long time. With the advance of digital electronics, the waveform of signals can be sampled, processed in the cards, possibly transferred to be processed in computer farms, even stored on disk for complex offline analysis. While traditional methods could still be implemented, digital electronics have also opened the path to new discrimination techniques (see [9,10] and references therein). As computation power becomes more affordable, machine learning techniques have emerged offering new possibilities

for offline as well as for online data processing. Concerning liquid scintillator detectors, it has been shown that artificial neural networks can improve n/γ discrimination especially at low energy [11,12]. For other scintillators, unsupervised algorithms have been found capable of separating γ -rays from neutrons and were also found useful to optimize parameters of traditional methods [13].

For many years, the AGATA germanium array has been installed at different facilities [14–16] and, for the first time, it was coupled at GANIL with the scintillators of the neutron array NEDA (including some modules of the Neutron Wall [17,18]) and with DIAMANT [19], a charged-particle detector array, see also [20]. The n/γ discrimination in the NEDA scintillators using three different types of Artificial Neural Networks (ANN) is reported here. Section 2 describes the experimental setup and introduces the ANN that were studied. Section 3 provides details on the implementation of such ANN and presents the results achieved on experimental data. The last Section 4 presents some complementary studies on pseudodata in order to highlight the differences between the different ANN architectures.

* Corresponding author.

E-mail address: o.stezowski@ip2i.in2p3.fr (O. Stézowski).

2. Methodology

2.1. Experimental context: 2018 AGATA -NEDA-DIAMANT campaign

The data used in this paper comes from one of the experiments carried out at GANIL in 2018 using the AGATA-NEDA-DIAMANT setup to detect in coincidence γ -rays, neutrons and charged particles. A beam of ^{50}Cr impinged on a target of ^{58}Ni at 175 MeV producing, through fusion-evaporation reactions, many different residual nuclei which can be characterized by the three detection systems.

At the lowest level, waveforms produced by the NEDA modules have been processed in the NUMEXO2 board, as explained in Ref. [21], and then sent to computer farms for more complex PSD. On the AGATA side, waveforms have been passed through the standard processing chain, the most important brick being the Pulse Shape Analysis (PSA) algorithm, to produce, for every single germanium crystal, a list of hits. Both subsystems were part of the Global Trigger and Synchronization system (GTS tree [22]) set up to validate or reject the events to be recorded. For the data used in this paper, the global trigger condition was one neutron identified in the NEDA cards (using a standard, fast algorithm) and one γ -ray on the AGATA side. For valid events, the NEDA waveforms were sampled every 5 ns over a window 1160 ns large and then recorded allowing to re-process the data through various PSD algorithms. A time of flight evaluation is also performed using the TDC implemented in the NUMEXO2 cards, the time reference being provided by the cyclotron RF signal, and the obtained value incorporated in the data flow. On the AGATA side, hits produced online by the PSA algorithm have been recorded. It should be noticed that such a choice for the global trigger condition does not have consequences on the results presented in this paper since only relative comparisons are performed. Triggerless data have also been recorded for a short time to allow absolute measurements. Indeed, such a triggerless acquisition produced a huge amount of data and unfortunately not enough coincidences to be statistically significant for the studies realized in this paper. Concerning DIAMANT, the standard parameters (energy and particle identification) from all the individual cells were recorded with the timestamp provided by the GTS system.

At the global level, coincidences were built offline using a window of 1 μs on timestamp data, before running the tracking algorithm on AGATA hits. A more precise window of 200 ns has been set at the very last stage of the data analysis. A particular attention has been devoted in having the three subsystems (AGATA-NEDA-DIAMANT) well aligned in time among each other to reduce random coincidences. For the NEDA subsystem itself, the time-alignment procedure has not been pushed to the finest level in order to stress the ANN with a greater variety of waveforms.

2.2. Artificial neural networks

For any given NEDA detector module, our goal was to provide the most efficient ANN able to answer the question whether or not the collected signal comes from a neutron. Thus our approach has been to feed the network not only with the waveform but also with the measured Time of Flight (T_{oF}) value. This differs from the previous studies [11,12] in which the discrimination is based only on samples of the signal. Feature extractions, the equivalent for machine learning approaches to calibration for physicists, is crucial to not spoil the performances of the ANN as it is going to be underlined in this paper: our choice has thus been to try and feed the networks with what we thought to be the more discriminant and the less noisy data. The input layer of the three ANN was composed of 75 neurons. On the first 73 neurons, samples of the waveform are given, the baseline being subtracted and the highest value normalized to 1. This represents a sampling of the scintillation light over 365 ns, which is long enough to include some background noise at the beginning (baseline) and to cover most of the collected signal especially the decay part, the most

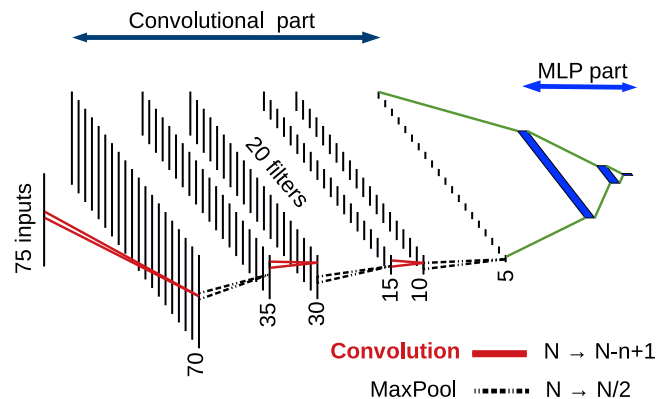


Fig. 1. (Color online) Convolutional neural network architecture used in this work. Twenty filters are applied to the 75 input data. Three consecutive convolutional layers are applied, each of them immediately followed by a max-pooling layer. N is at each step the number of inputs while n is the size of the kernel (see text for further explanations). Data are then flattened to feed a MLP (sequence of fully connected layers) architecture.

relevant one for the discrimination. Since a single ANN has been used whatever the NEDA module, all the detectors have been aligned so that the true collected signal starts at about 80 ns. On neurons 74 and 75 are given respectively the amplitude of the signal, so that the network can deal with energy depositions, and the T_{oF} value.

The last layer is composed of two neurons because there are two classes: neutron or not a neutron (by extension abusively labeled γ -ray). For consistency, the sum of the two output values is always equal to 1 because of the renormalized exponential *softmax* activation function being used. The first (second) output neuron thus yields the probability that the given waveform is generated by a neutron (γ -ray). The differences and parameters used to setup the three different ANN studied are summarized in Table 1.

The first architecture, a Multi Layer Perceptron (MLP), is similar to the one proposed by Ronchi et al. [11]: neurons are fully connected between consecutive layers and we have used two hidden layers. We reduced the size of the two hidden layers from 20 and 5 neurons to 10 and 4 respectively as it led to similar results. The second architecture, a Convolutional Neural Network (CNN), usually takes images as input upon which features are extracted at different zoom/scale levels. The one-dimensional image provided in this work to this ANN was the sampled waveform. The CNN architecture is made of three convolution layers each of them immediately followed by a max-pooling layer (see Fig. 1) which reduces by a factor of 2 the size of the input by keeping the highest (*max*) of two consecutive inputs. The size of all the filters (kernels) used has been set to six which corresponds, at least for the input layer, to search (through the convolution product) for features in the signal over a 60 ns time window. We have set the number of filters to 20. The last layer of the convolutional part is connected to a MLP, i.e. a sequence of fully connected layers, composed respectively of 100, 20 and 2 neurons. The third architecture studied is based on Long Short Term Memory (LSTM) layers [23], an evolution of the Recurrent Neural Network architecture. For such a kind of layer, inputs are fed by time steps, along with the output of the previous time step. An important parameter is the number of memory units used to pass information from one time step (sample i of the waveform) to the next one (sample $i + 1$ of the waveform). This number of units also set the number of output values of the LSTM layer. The LSTM architecture is able to select which information will be forgotten or added, giving better results in applications where the context is important. Since in our case the discrimination is done looking at the way the decay part of the signal evolves, our strategy has been to have an LSTM layer, to try and extract the time evolution, coupled with a MLP layer to do the discrimination. For the architecture studied in the work, we have chosen only one LSTM

layer composed of 50 units giving then 50 output values fully connected to the output layer composed of the two neurons used for neutron/ γ classification.

ANN are supervised machine learning algorithms: the training/validating phase is crucial to get an efficient and robust classifier. For the three proposed architectures, the hyperparameters of the networks (number of layers, number of neurons per layer, ...) have been tuned to find the most compact structure in order to minimize the online processing time. Large networks have been set and trained to reach the highest accuracy. The hyperparameters have then been modified to decrease the size of the networks. The selected ANN can be trained within few hours (on our GPU card) to reach the accuracy obtained with bigger ANNs.

The training/validation datasets have been prepared from the data collected during the experiment. First, signals have been cleaned by removing pile-up events and badly shaped waveforms. This procedure has been based on a standard algorithm which consists in keeping only signals having one zero-crossing in their first derivative. Several two dimensional cuts have been used to tag a signal as coming from neutrons or γ -rays. The involved quantities to build the 2D histograms are the time of flight ToF , the amplitude of the waveform and a parameter called Slow on Fast SoF . The SoF parameter, described in Ref. [11], implements the charge comparison method by calculating the ratio between the integration of the waveform before and after a time boundary. Fig. 2 shows ToF - SoF density plots.

The black cut contains mostly neutrons while the red one is used to tag γ -rays or any event which obviously cannot be assigned to a single clean neutron. It should be noticed that there is a region in between containing events not used at the training/validation level. Such events are precious to check the ANNs behave consistently and to look for any overfitting. We will address this point in the next section. Similar 2D plots have been built using the ToF and the amplitude of the waveform in which specific 2D cuts have been drawn to distinguish neutrons from γ -rays/backgrounds. The conjunction (*and* operator) of the 2D cuts determines whether or not a signal should be tagged as neutron or not a neutron. While the complete procedure allows to strongly tag a signal as coming from a neutron or even a γ -ray, it does not however exclude the possibility to have a fraction of mislabels.

For the training phase, the data set (140000 signals) we used was composed of an equal number of neutrons (70000 signals) and γ -rays (70000 signals). The signals were randomly dispatched in two groups: 90% of them to train the network and 10% for validation. At each epoch, the accuracy of the network is calculated for the training and for the validation data set to look, at this level, for any overfitting. Using only the accuracy on the validation data set, the training phase is stopped once this value is not progressing over 20 epochs. For the studies we performed in this paper, the network having the best accuracy over the last 20 epochs is applied to a different data set itself composed of 5.7 million of events (two different runs). For the training phase, we have used a standard categorical cross-entropy loss function which is well suited to single label categorization problems. Regarding the optimizer, the MLP and CNN architectures are trained using a Stochastic Gradient Descent algorithm while the Adam algorithm led to a faster training for the LSTM network.

2.3. Figures of merit

Once an artificial neural network is trained, one can use it to classify any detector fired in NEDA as likely to have been impinged by a neutron or by a γ -ray. The output of the network (*Neural Network Output Value*) is embedded in the data flow of the data acquisition system.

In this paper, in order to compare the three networks, we will normalize it such that the value is inside [0;100] (*NNNOV* for *Normalized Neural Network Output Value*). For any event, whatever the PSD algorithm, NEDA provides a counting on the number of neutrons (xn) detected which allows, from the tracked γ -ray in coincidence in AGATA,

Table 1

Consecutive layers (second column) composing the three different neural network architectures (first column) and their number of parameters (third column). D, C, M, R and F means respectively Dense, Convolutional, Max pooling, Recurrent and Flatten layer.

Network	Layer structure	# of parameters
MLP	75:D:10:D:4:D:2	814
LSTM	75:R:50:D:2	10 502
CNN	75:(C:70:M:35:C:30:M:15:C:10:M:5)x20 F:100:D:20:D:2	7042

to build the different γ -ray spectra (S^{xn}) associated to the number of neutrons identified (xn).

Through the γ -ray transitions in those spectra we do have a way to determine how many neutrons are emitted, assuming a clean γ -ray transition is well selected. Combining all the information one can extract a *mislabel probability*, i.e. the probability to incorrectly qualify an event, as detailed in Appendix. Of course, increasing the selectivity of any condition, whatever the algorithm, results in less *statistics* in the channel of interest and this has to be evaluated in balance with the *mislabel probability*.

The performances of the three ANN architectures have been compared with respect to a more classical approach consisting in tagging a signal with the conjunction of the two 2D cuts that have been defined to train the networks. To get a clean spectrum, we have restricted our studies to events having only one NEDA module fired and we have required to have three protons detected and zero alpha detected in DIAMANT. This leads to study the ^{105}In and ^{104}In nuclei which correspond respectively to 0 and 1 neutron emitted.

The γ -ray transitions selected to estimate the *mislabel probability* and the *gain/loss in statistics* are at high energy in the γ -ray spectrum where the density of transitions is also reduced. Our final choice has been set on the 1341.6 keV ($\frac{13}{2}^+ \rightarrow \frac{9}{2}^+$) and the 1258.8 keV ($9^+ \rightarrow 7^+$) γ -ray transitions respectively corresponding to the 0 and 1 neutron evaporation channel.

3. Results on experimental data

3.1. Implementation

As explained in Ref. [2], whatever the algorithm, the Pulse Shape Discrimination should be applied online to reduce as soon as possible the transfer of data. At this level in the data flow, waveforms are reduced to a few parameters, in particular one tagging the event as coming from a γ -ray or a neutron. While waveforms can also be stored on disk at an earlier stage for offline re-processing, it is however obvious that any PSD in NEDA should be compliant for online processing which puts stringent constraints on the technological solution used to run machine learning based algorithms. To fully benefit from the multiple CPU and multi-core machines of the NEDA computer farm, our choice has been to use the TensorFlow library [24] which allows a high level parallelization, provides a C++ interface and can run either on CPU or on GPU. The ANNs have been trained using the Keras [25] python interface. Typical time to train an ANN, i.e. to reach a target accuracy of about 98% without improvement on the validation dataset over 20 epochs, is 30 minutes and 60 minutes for the MLP/LSTM and CNN architecture respectively on our hardware.

Once frozen, the ANN model is uploaded in a NARVAL actor (see Ref. [2]) to process any signal out of the NEDA modules. To fully take advantage of the parallelism capabilities of the TensorFlow Library, waveforms are first grouped by batches before being processed by the library. Typical inference times have been estimated for the three ANNs we have studied. They are given in Table 2 for different batch sizes and different processing units. The batch size may have a significant

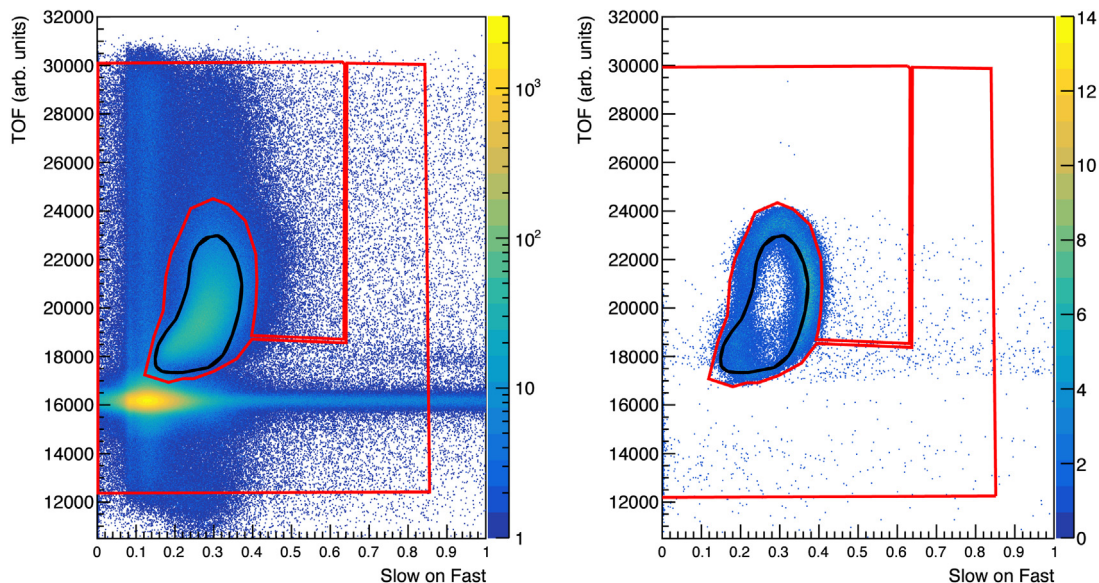


Fig. 2. Time Of Flight ToF versus Slow On Fast SoF for all events (left side) and for a subset of events selected by the MLP network output value (right side). The black line represents the cut used at training time to tag neutrons while the red one is for γ -rays. (For interpretation of the references to color in this figure legend, the reader is referred to the web version of this article.)

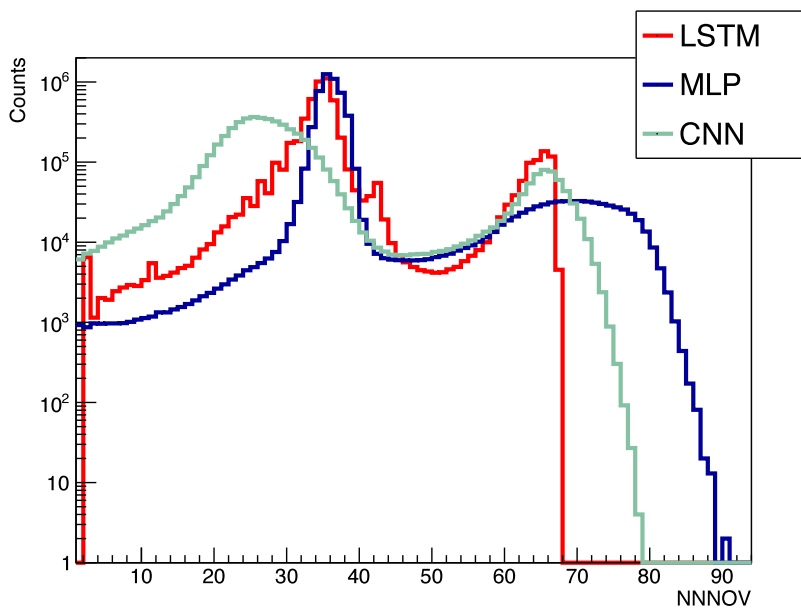


Fig. 3. (Color online) Normalized Neural Network Output Value $NNNOV$ distributions for the three ANN architectures.

impact on the mean processing time for a single event and should be selected accordingly. As it can be seen, the MLP architecture is the fastest with about $1 \mu s$ inference time, whatever the computing unit. With such a time, we were able, during the full AGATA-NEDA-DIAMANT campaign, to perform inference online (on CPU units), using such neural network architecture at a mean maximum rate of about 6500 Hz at the PSD level. The two other architectures have been developed after the campaign and thus have not been tested online in a complex environment. Inference times on CPU are at least ten time slower. It may have been a bottleneck of the data processing chain, bottleneck that could be absorbed, at least partially, at the cost of running online with GPU cards in the DAQ box.

3.2. Mislabeled and statistics

Fig. 3 gives the Normalized Neural Network Output Value $NNNOV$ distributions obtained for the three different architectures. For all the

Table 2

Typical inference times (in μs per signal) for the three ANNs depending on the batch size and the processing unit used.

Batch Size	MLP		CNN		LSTM	
	CPU	GPU	CPU	GPU	CPU	GPU
5000	1.5	0.7	9.5	1.8	50.0	12.0
20 000	1.0	0.7	11.0	1.7	60.0	10.0
80 000	1.2	0.8	11.0	4.0	75.0	9.0

distributions, one can clearly see two peaks. The first one (low values) corresponds to input classified as γ -rays and the second one (high values) corresponds to neutrons. One can see different behaviors by comparing the resolutions of the peaks. The peaks of the CNN distribution are the broadest suggesting the network is less clear concerning the way it classifies. On the other hand, the LSTM distribution provides

well defined, sharp peaks while it is the case only for γ -rays looking at the MLP output. The regions in between the two main peaks suggest also the LSTM network is more confident in its classification than the others.

A threshold $NNNOV_{thn}$ on the distribution provides a way to classify an input as neutron ($NNNOV \geq NNNOV_{thn}$) or γ -ray ($NNNOV < NNNOV_{thn}$). Depending on the analysis one would like to perform, one can then be more or less restrictive. Because the networks take as input the whole signal, and the T_oF , moving the threshold is equivalent to increasing/decreasing the boundaries of complex cuts in a multidimensional space. It goes also beyond the basic application of the 2D cuts that have been used to tag the training inputs. For instance, a selection by the output of the network of γ -ray events allows to get some events inside the black cut shown in Fig. 2: those events are related, as expected, to background under the island of neutrons.

The classification provided by the networks might be wrong. As explained in Section 2.3, through the γ -rays detected in coincidence in AGATA one can evaluate how wrong the n/γ discrimination is through the *mislabeled probability*. Fig. 4 shows, for the three ANN, the evolution of the *mislabeled probability* as a function of the threshold $NNNOV_{thn}$ applied. To complete the comparisons, the *mislabeled probability* for a discrimination based only on the training cuts is also given. With our data and cuts, we got about 1.2%, which corresponds to the horizontal blue line in Fig. 4. The *gain/loss in statistics* is also given (in red) relative to the basic application of the training cuts. As expected, increasing the threshold results in having less mislabeled events. The cost is of course less statistics for the selected events. The three ANN have a similar global behavior and cross the horizontal lines at slightly different values. At the crossing points $NNNOV_{thnc}$, the ANN have the same performances than the standard 2D cuts. Note that the numbers given here for the quality of the neutron-gamma discrimination using the charge comparison method are valid only for the cuts used in the training, and do not reflect true limits of the NEDA array [G. Jaworski et al. to be published]. With a threshold ($NNNOV_{thn} = 52$) lower than the crossing point ($NNNOV_{thnc} = 58$), one can get, for the MLP architecture, the blue spectrum displayed in Fig. 5. It is compared with what is obtained by applying only the 2D cuts (gray spectrum). One can see there are more counts in all the peaks, in the expected γ -ray transitions coming from the one neutron evaporation channel (1258.8 keV, $9^+ \rightarrow 7^+$ ^{104}In) but also in the background one (1341.6 keV, $\frac{13^+}{2} \rightarrow \frac{9^+}{2}$ ^{105}In). This is expected since the *Mislabeled probability* evolves slowly before the crossing point. With a threshold higher than the crossing point ($NNNOV_{thn} = 64$) the red spectrum is obtained. Looking at the 1341.6 keV ($\frac{13^+}{2} \rightarrow \frac{9^+}{2}$ ^{105}In) transition, the reduction of the background transitions due to the higher neutron selectivity becomes visible. At the same time, counts in the interesting peaks are also well reduced. This analysis bolsters our confidence that the output of the ANN is a good marker for a precise neutron selection in NEDA.

The last point we have checked is how the networks are able to interpolate on inputs that have not been part of the training set (see Section 2). Indeed, specific cuts have been used to tag neutrons (see black contour in Fig. 2) and γ -rays (red contour in Fig. 2). The three networks have consistently characterized such an unlabeled category: the bulk of events in between the cuts are classified with *Normalized Neural Network Output Value* between 40 and 60, i.e. between the main peaks corresponding to γ -rays and neutrons. Such capability to interpolate is illustrated in Fig. 2 where one can see the distribution of inputs having, for the MLP architecture, a *Normalized Neural Network Output Value* in the range 40 to 60. A polynomial fit (order 3) of the *mislabeled probability curve* in that range has shown that the inflection point of the curve matches almost the position of the lowest points in the valley of the *Normalized Neural Network Output Value* distribution. As already pointed out, this valley is deeper for the LSTM architecture. In order to see whether or not such architecture outperforms the other ones, we have realized complementary studies using synthetic pulses instead of real data.

4. Results on pseudodata

The ANNS slightly differ in their response function and their capabilities to interpolate. In order to understand how sensitive they are to the input, we have generated synthetic pulses instead of real data. This has two main advantages:

- there are no ambiguities at all concerning the nature of the particles generating the waveforms used for training;
- the shape of the signal is parameterized and all the parameters are completely known.

In the following sections, the procedure to produce signals is first given and then the sensitivity to some parameters is explored.

4.1. Waveform generation

We have used the Marrone's model which describes scintillator pulse shapes as (see [11])

$$s(t) \propto \left[\exp\left(-\frac{t-T_0}{\theta}\right) - \exp\left(-\frac{t-T_0}{\lambda_s}\right) + R \exp\left(-\frac{t-T_0}{\lambda_l}\right) \right] \quad (1)$$

where θ , λ_s and λ_l are different specific decay times, in principle constant for a given material. T_0 , the time at which the signal starts, experimentally depends on the way the electronic card captures the waveform. The interaction of neutrons with liquid scintillator detectors produces more excited molecular states with long decay times than γ -rays. Since the R parameter in Eq. (1) controls the proportion of the longest decay time (λ_l) to the signal, it is directly connected to the nature of the interacting particle.

In order to set parameters which are as realistic as possible, clean signals from real NEDA detectors have been fitted with the function and the parameters extracted from the parameters distributions obtained. It leads to set θ to 16 ns, λ_s to 20 ns and λ_l to 270 ns. Sensitivities to R and T_0 have been tested and values have been set differently depending on the objectives. However, the mean value of R has been set from the fits to $R_{mean-n} = 0.0415$ for neutrons and $R_{mean-\gamma} = 0.0165$ for γ -rays. Once the parameters are fixed, two histograms are built, one for neutrons and one for γ -rays with a binning corresponding to the sampling of the real signals. The signals required for the ANNS training/validating/testing are then randomly generated. The full procedure is to first select the nature of the particle (equal number of neutrons and γ -rays), to set the integral I_s (constant and equal to the mean value of the real signals) and the T_0 (from the relevant Gaussian distribution) of the signal, and then to randomly produce I_s values from the corresponding histogram: this allows the inclusion of some random statistical noises, quite similar to the real ones even if a bit smaller, to the generated waveforms. One should mention however that this level of noise remains quite low and does not affect the general conclusions given in Section 4.2.

4.2. Sensitivity to input parameters R and T_0

The first parameter we have played is R with T_0 constant and equal to 80 ns. Signal by signal, R has been randomly set using Gaussian distributions centered respectively on $R_{mean-n} = 0.0415$ for neutrons and $R_{mean-\gamma} = 0.0165$ for γ -rays. The widths of the distributions σ_n and σ_γ have been modified so that for some studies the two distributions are clearly separated while for others they overlap. What we have observed is, whatever the ANN architecture, the network, once trained, is able to recognize a γ -ray from a neutron with almost 100% efficiency as soon as the neutron distribution is well separated from the γ -ray one. In case of overlapping, the three networks are wrong in about 50% of the cases for signals in the overlapping area. This is of course expected. For the second study, the two widths for the R Gaussian distributions have been set respectively to $\sigma_n = 0.0013$ and $\sigma_\gamma = 0.001$, so that the two distributions do not overlap. The signals for the training have been generated using a Gaussian distribution for T_0 with a σ of 2 ns. The

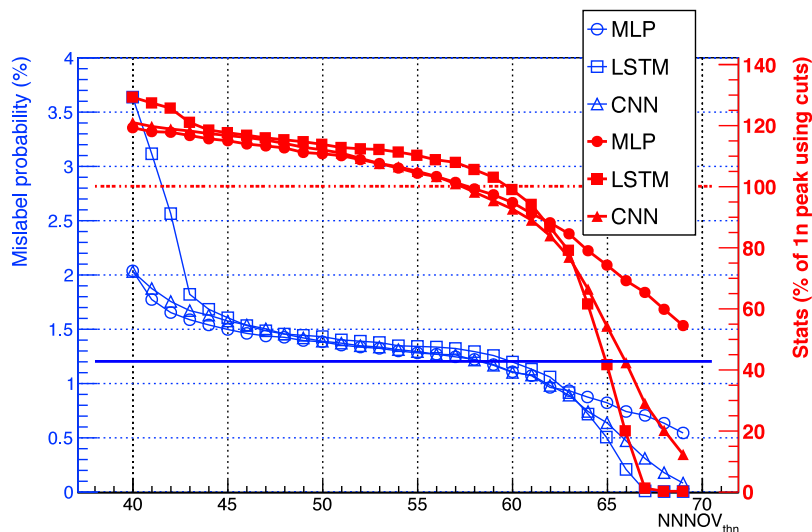


Fig. 4. Mislabeled probability (in blue) and statistics (in red) for the three ANN architectures as a function of the threshold $NNNOV_{thn}$ applied to the Normalized Neural Network Output Value $NNNOV$. The horizontal lines correspond to the results obtained by applying a discrimination based only on standard binary cuts, the ones used to train the networks. (For interpretation of the references to color in this figure legend, the reader is referred to the web version of this article.)

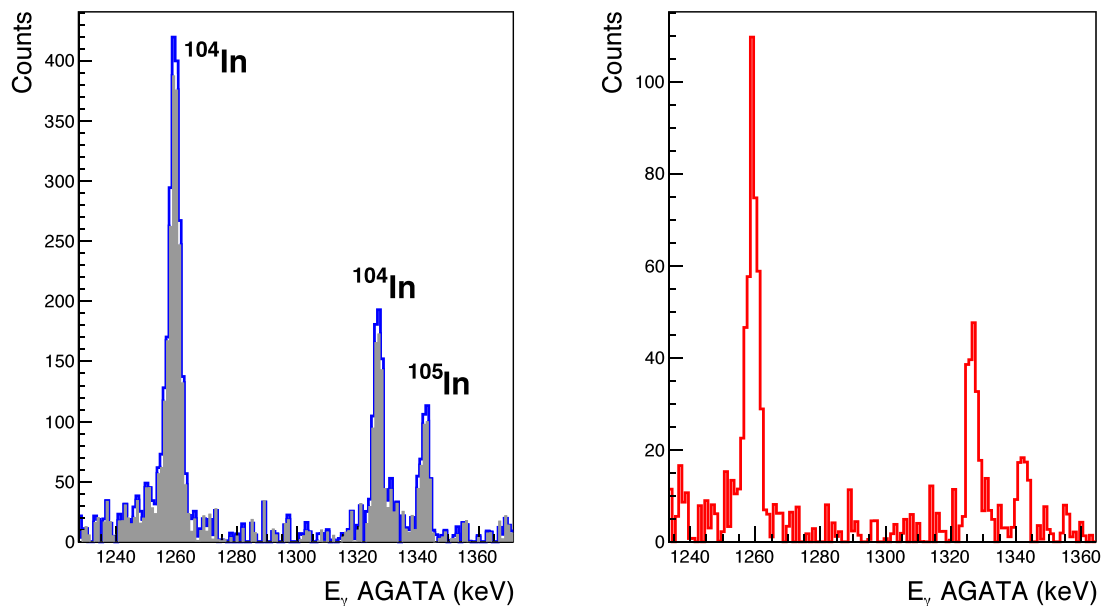


Fig. 5. Part of AGATA γ -ray spectra obtained by setting different conditions on NEDA. In blue by applying a threshold ($NNNOV_{thn} = 52$) on the Normalized Neural Network Output Value slightly lower than $NNNOV_{hnc} = 58$ which corresponds in Fig. 4 to the crossing point between the horizontal blue line and the MLP Mislabeled probability curve. In gray by applying classical 2D cuts, the ones used to train the networks. In red by applying a threshold ($NNNOV_{thn} = 64$) on the Normalized Neural Network Output Value higher than $NNNOV_{hnc} = 58$. (For interpretation of the references to color in this figure legend, the reader is referred to the web version of this article.)

networks have then been tested with three set of signals generated by broadening the T_0 distribution respectively with $\sigma = 10$ ns, $\sigma = 20$ ns and $\sigma = 40$ ns. Such a procedure is performed to check the sensitivity of the network to misalignment of the signals, which is likely to happen during an experiment. We have quantified the percentage of signals for which the classification done by the three networks is reliable, i.e. when the range in the Normalized Neural Network Output Value for which the distribution coming from neutrons overlaps with the one from γ -rays is excluded. The results are given in picture 6. Obviously, the performances of the LSTM network are not affected at all by any shift in time of the input signals. This is certainly inherent to such networks for which correlations in the input sequence are explored. Such a characteristic is of great interest for online processing, this would allow to have an algorithm that can operate with the same efficiency in case any time misalignment occurs. The CNN architecture

remains efficient but only to some extent. For that network, it should be noticed that there might be different combinations of hyper parameters that could possibly reach the raw performances of the LSTM network. The MLP architecture is the worst: the loss in efficiency reaches quickly 50% as soon as the width of the T_0 distribution is increased. In fact, the discrimination for that network relies mostly on a particular sub-range of input values (the decay part which is the part of the signal different for both particles). For instance, setting to 0 the rising part of the signals modifies only slightly the MLP performances. It is thus crucial to feed this network only with well aligned signals, at least signals similar to the waveforms used for the training part.

Closely related to this behavior, we would like to mention other studies we have performed concerning the performances of the three architectures to identify and disentangle pile-up signals. The full studies are out of the scope of the present article. However, one could mention

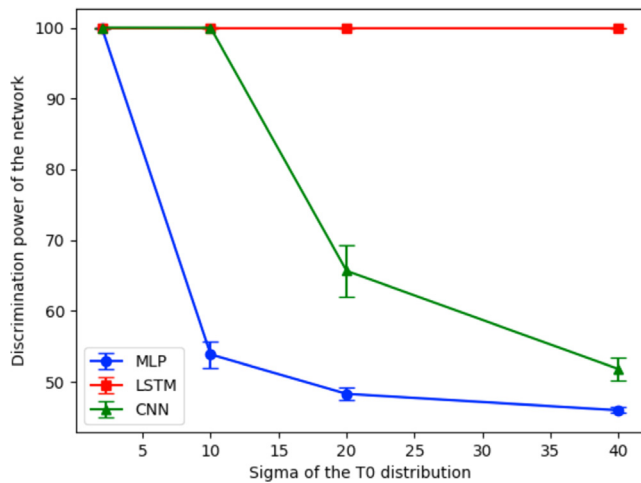


Fig. 6. (Color online) Discrimination power of the three different ANN architectures as a function of the σ of the T_0 Gaussian distribution used to generate the signals and test the networks.

that, as it is the case for the studies on sensitivity to the T_0 parameter, the MLP architecture has been found less capable of identifying pile-up in cases where the two signals have very close T_0 values.

5. Conclusions

Different ANN architectures have been tested to perform n/γ discrimination in the NEDA neutron detector. Thanks to the coupling with the AGATA γ -ray detector, we have been able to quantify and qualify precisely the performances of the networks compared to a more classical approach based on binary cuts. Thresholds on a unique parameter, the output of the network, are equivalent to apply complex cuts to select neutrons. The interpolation capabilities of the networks have also been shown to be correct. Using the TensorFlow library, online inferences on CPU based machines have been performed for the MLP architecture. The three ANNs slightly differ in their way of classifying the input data. One explanation is the sensitivity of the networks to the misalignment of the input waveform. On this point, the LSTM architecture is extremely robust such that it embodies the preferred candidate for online processing. On the other hand, inference for such architectures needs more processing time, which may impose the use of GPU cards. Like for more classical discrimination algorithms, calibration (feature extraction), may deteriorate the global performances of the ANN if the chosen solution is too sensitive to parameters likely to be unstable. One solution offered by machine learning techniques would be to use autoencoders in order to identify, signal by signal, anomalies so that the most adapted algorithm could be applied.

CRediT authorship contribution statement

X. Fabian: Formal analysis, Software, Methodology, Visualization, Data curation, Validation. **G. Baulieu:** Conceptualization, Formal analysis, Software, Methodology, Visualization, Data curation. **L. Ducroux:** Formal analysis, Software, Methodology, Data curation, Validation. **O. Stézowski:** Conceptualization, Formal analysis, Software, Methodology, Writing - original draft, Writing - review & editing. **A. Boujrad:** Investigation, Data curation, Resources. **E. Clément:** Investigation, Data curation, Resources. **S. Coudert:** Investigation, Data curation, Resources. **G. de France:** Investigation, Data curation, Resources. **N. Erduran:** Investigation, Data curation, Resources. **S. Ertürk:** Investigation, Data curation, Resources. **V. González:** Investigation, Data curation, Resources. **G. Jaworski:** Investigation, Data curation, Resources. **J. Nyberg:** Investigation, Data curation, Resources. **D. Ralet:** Investigation, Data curation, Resources. **E. Sanchis:** Investigation, Data curation, Resources. **R. Wadsworth:** Investigation, Data curation, Resources.

Declaration of competing interest

The authors declare that they have no known competing financial interests or personal relationships that could have appeared to influence the work reported in this paper.

Acknowledgment

One of the author acknowledges support of the National Science Centre, Poland (NCN) (grant no. 2017/25/B/ST2/01569).

Appendix. Conditional and mislabel probabilities

With NEDA and AGATA in coincidence, one can build γ -ray spectra as a function of the number of neutrons detected (and classified as such). This is illustrated in Fig. A.1. The horizontal axis represents γ -ray energies detected on which are shown several γ -ray transitions ($\gamma^{0n}, \gamma^{1n}, \dots, \gamma^{yn}$) that unambiguously identify a given nucleus using its level scheme. The superscript is thus related to the number of neutrons emitted by the compound nucleus to feed a particular residue. γ -ray spectra (S^{xn}) are decomposed on the second axis depending on the number of neutrons detected (xn). On the vertical axis one can read the intensity of the measured γ -ray lines. For a given γ -ray line, the sum of all the intensities over the different spectra is constant and can be used to calculate several conditional probabilities. $p(xn|yn)$, the conditional probability to detect (and identify as such) x neutrons knowing that y are emitted, is given by

$$p(xn|yn) = \frac{I^{S^{xn}}(\gamma^{yn})}{\sum_{xn=0}^{\infty} I^{S^{xn}}(\gamma^{yn})} \quad (\text{A.1})$$

The intensities on the diagonal of the matrix ($x = y$) are related to the efficiency of the NEDA array. In particular, for the case $x = y = 1$, one

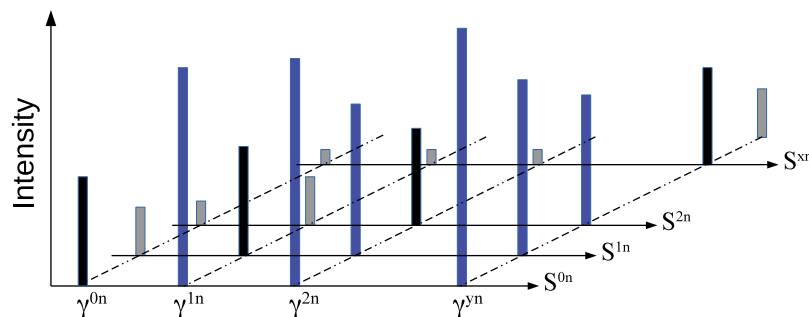


Fig. A.1. (Color online) Schematic matrix showing the intensity of the γ -ray lines γ^{yn} corresponding to yn neutrons emitted decomposed into different spectra, S^{xn} corresponding to the number of neutrons xn detected and classified as neutron in NEDA.

can get the efficiency to select the one neutron evaporation channel. Probabilities from under the diagonal (less neutrons detected than emitted) are due mostly to the geometrical efficiency since the detector does not cover 4π . It includes also the probability to identify a neutron as a γ -ray. This number however should be marginal since much more γ -ray are emitted and interact with the detector than neutrons. More interesting for this paper are the intensities over the diagonal: they are due to neutron crosstalks (the same neutron hits several modules) as well as wrong classifications i.e. γ -rays identified as neutrons. Looking at events where only one NEDA module has fired removes the contribution of the cross-talks. Thus the conditional probability $p(1n|0n)$ to detect one neutron knowing that no neutron has been emitted, can be used as a measurement of the *mislabeled probability* due to the classifier.

$$\text{mislabeled probability} = p(1n|0n) = \frac{I^{S^{1n}}(\gamma^{0n})}{\sum_{xn=0}^{\infty} I^{S^{xn}}(\gamma^{0n})} \quad (\text{A.2})$$

References

- [1] T. Hüyük, A. Di Nitto, G. Jaworski, A. Gadea, J. Javier Valiente-Dobón, J. Nyberg, M. Palacz, P.-A. Söderström, R. Jose Aliaga-Varea, G. de Angelis, A. Ataç, J. Collado, C. Domingo-Pardo, F.J. Egea, N. Erduran, S. Ertürk, G. de France, R. Gadea, V. González, V. Herrero-Bosch, A. Kaşkaş, V. Modamio, M. Moszynski, E. Sanchis, A. Triossi, R. Wadsworth, Conceptual design of the early implementation of the NEutron Detector Array (NEDA) with AGATA, *Eur. Phys. J. A* 52 (3) (2016) 55, <http://dx.doi.org/10.1140/epja/i2016-16055-8>.
- [2] J. Valiente-Dobón, G. Jaworski, A. Goasduff, F. Egea, V. Modamio, T. Hüyük, A. Triossi, M. Jastrzab, P. Söderström, A.D. Nitto, G. de Angelis, G. de France, N. Erduran, A. Gadea, M. Moszynski, J. Nyberg, M. Palacz, R. Wadsworth, R. Aliaga, C. Aufranc, M. Bézard, G. Baulieu, E. Bissiat, A. Boujrad, I. Burrows, S. Carturan, P. Cocconi, G. Colucci, D. Conventi, M. Cordwell, S. Coudert, J. Deltoro, L. Ducroux, T. Dupasquier, S. Ertürk, X. Fabian, V. González, A. Grant, K. Hadyńska-Klek, A. Illana, M. Jurado-Gomez, M. Kogimtzis, I. Lazarus, L. Legeard, J. Ljungvall, G. Pasqualato, R. Pérez-Vidal, A. Raggio, D. Ralet, N. Redon, F. Sallant, B. Saygı, E. Sanchis, M. Scarciuffolo, M. Siciliano, D. Testov, O. Stezowski, M. Tripón, I. Zanon, NEDA—Neutron detector array, *Nucl. Instrum. Methods Phys. Res. A* 927 (2019) 81–86, <http://dx.doi.org/10.1016/j.nima.2019.02.021>, URL <http://www.sciencedirect.com/science/article/pii/S0168900219301962>.
- [3] S. Akkoyun, A. Algora, B. Alikhani, F. Ameil, G. de Angelis, L. Arnold, A. Astier, A. Ataç, Y. Aubert, C. Aufranc, A. Austin, S. Aydin, F. Azaiez, S. Badoer, D. Balabanski, D. Barrientos, G. Baulieu, R. Baumann, D. Bazzacco, F. Beck, T. Beck, P. Bednarczyk, M. Bellato, M. Bentley, G. Benzoni, R. Berthier, L. Berti, R. Beunard, G.L. Bianco, B. Birkenbach, P. Bizzeti, A. Bizzeti-Sona, F.L. Blanc, J. Blasco, N. Blasi, D. Bloor, C. Boiano, M. Borsato, D. Bortolato, A. Boston, H. Boston, P. Bourgault, R. Boutachkov, A. Bouty, A. Bracco, S. Brambilla, I. Brawn, A. Brondi, S. Broussard, B. Bruyneel, D. Bucurescu, I. Burrows, A. Bürger, S. Cabaret, B. Cahán, E. Calore, F. Camera, A. Capsoni, F. Carrió, G. Casati, M. Castoldi, B. Cederwall, J.-L. Cericus, V. Chambert, M.E. Chambit, R. Chapman, L. Charles, J. Chavas, E. Clément, P. Cocconi, S. Coelli, P. Coleman-Smith, A. Colombo, S. Colosimo, C. Commeaux, D. Conventi, R. Cooper, A. Corsi, A. Cortesi, L. Costa, F. Crespi, J. Cresswell, D. Cullen, D. Curien, A. Czermak, D. Delbourg, R. Depalo, T. Descombes, P. Désesquelles, P. Destivou, C. Diarra, F. Didierjean, M. Dimmock, Q. Doan, C. Domingo-Pardo, M. Doncel, F. Dorangeville, N. Dosme, Y. Drouen, G. Duchêne, B. Dulny, J. Eberth, P. Edelbruck, J. Egea, T. Engert, M. Erduran, S. Ertürk, C. Fanin, S. Fantinel, E. Farnea, T. Faul, M. Filliger, F. Filmer, C. Finck, G. de France, A. Gadea, W. Gast, A. Geraci, J. Gerl, R. Gernhäuser, A. Giannatiempo, A. Giaz, L. Gibelin, A. Givechev, N. Goel, V. González, A. Gottardo, X. Grave, J. Grebosz, R. Griffiths, A. Grint, P. Gros, L. Guevara, M. Gulmini, A. Görger, H. Ha, T. Habermann, L. Harkness, H. Harroch, K. Hauschild, C. He, A. Hernández-Prieto, B. Hervieu, H. Hess, T. Hüyük, E. Ince, R. Isocrate, G. Jaworski, A. Johnson, J. Jolie, P. Jones, B. Jonson, P. Joshi, D. Judson, A. Jungclaus, M. Kaci, N. Karkour, M. Karolak, A. Kaşkaş, M. Kebbiri, R. Kempley, A. Khaplanov, S. Klupp, M. Kogimtzis, I. Kojouharov, A. Korichi, W. Korten, T. Kröll, R. Krücken, N. Kurz, B. Ky, M. Labiche, X. Lafay, L. Laverne, I. Lazarus, S. Leboutelier, F. Lefebvre, E. Legay, L. Legeard, F. Lelli, S. Lenzi, S. Leoni, A. Lermitege, D. Lersich, J. Leske, S. Letts, S. Lhenoret, R. Lieder, D. Linget, J. Ljungvall, A. Lopez-Martens, A. Lotodé, S. Lunardi, A. Maj, J. van der Marel, Y. Mariette, N. Marginean, R. Marginean, G. Maron, A. Mather, W. Meczyński, V. Mendéz, P. Medina, B. Melon, R. Menegazzo, D. Mengoni, E. Merchan, L. Mihailescu, C. Michelagnoli, J. Mierzejewski, L. Milechina, B. Million, K. Mitev, P. Molini, D. Montanari, S. Moon, F. Morbiducci, R. Moro, P. Morrall, O. Möller, A. Nannini, D. Napoli, L. Nelson, M. Nespolo, V. Ngo, M. Nicoletto, R. Nicolini, Y.L. Nolan, P. Nolan, M. Norman, J. Nyberg, A. Obertelli, A. Olariu, R. Orlandi, D. Oxley, C. Özen, M. Ozille, C. Oziol, E. Pachoud, M. Palacz, J. Palin, J. Pantic, C. Parisel, P. Pariset, G. Pascovici, R. Peghin, L. Pellegrini, A. Perego, S. Perrier, M. Petcu, P. Petkov, C. Petrache, E. Pierre, N. Pietralla, S. Pietri, M. Pignanelli, I. Piqueras, Z. Podolyak, P.L. Poughalec, J. Pouthas, D. Pugnère, V. Pucknell, A. Pullia, B. Quintana, R. Raine, G. Rainovski, L. Ramina, G. Rampazzo, G.L. Rana, M. Rebeschini, F. Recchia, N. Redon, M. Reese, P. Reiter, P. Regan, S. Riboldi, M. Richer, M. Rigato, S. Rigby, G. Ripamonti, A. Robinson, J. Robin, J. Roccaz, J.-A. Ropert, B. Rossé, C.R. Alvarez, D. Rosso, B. Rubio, D. Rudolph, F. Saillant, E. Şahin, F. Salomon, M.-D. Salsac, J. Salt, G. Salvato, J. Sampson, E. Sanchis, C. Santos, H. Schaffner, M. Schlarb, D. Scraggs, D. Seddon, M. Şenyiğit, M.-H. Sigward, G. Simpson, J. Simpson, M. Slee, J. Smith, P. Sona, B. Sowicki, P. Spolaore, C. Stahl, T. Stanios, E. Stefanova, O. Stézowski, J. Strachan, G. Suliman, P.-A. Söderström, J. Tain, S. Tanguy, S. Tashenov, C. Theisen, J. Thornhill, F. Tomasi, N. Toniolo, R. Touzery, B. Travers, A. Triossi, M. Tripón, K. Tun-Lanoë, M. Turcato, C. Unsworth, C. Ur, J. Valiente-Dobon, V. Vandone, E. Vardaci, R. Venturelli, F. Veronese, C. Veysiere, E. Viscione, R. Wadsworth, P. Walker, N. Warr, C. Weber, D. Weisshaar, D. Wells, O. Wieland, A. Wiens, G. Wittwer, H. Wollersheim, F. Zocca, N. Zamfir, M. Ziebliński, A. Zucchiatti, AGATA—Advanced gamma tracking array, *Nucl. Instrum. Methods Phys. Res. A* 668 (2012) 26–58, <http://dx.doi.org/10.1016/j.nima.2011.11.081>, URL <http://www.sciencedirect.com/science/article/pii/S0168900211021516>.
- [4] J. Qin, C. Lai, B. Ye, R. Liu, X. Zhang, L. Jiang, Characterizations of BC501A and BC537 liquid scintillator detectors, *Appl. Radiat. Isot.* 104 (2015) 15–24, <http://dx.doi.org/10.1016/j.apradiso.2015.06.008>, URL <http://www.sciencedirect.com/science/article/pii/S096980431530052X>.
- [5] F. Brooks, A scintillation counter with neutron and gamma-ray discriminators, *Nucl. Instrum. Methods* 4 (3) (1959) 151–163, [http://dx.doi.org/10.1016/0029-554X\(59\)90067-9](http://dx.doi.org/10.1016/0029-554X(59)90067-9), URL <http://www.sciencedirect.com/science/article/pii/0029554X59900679>.
- [6] J. Adams, G. White, A versatile pulse shape discriminator for charged particle separation and its application to fast neutron time-of-flight spectroscopy, *Nucl. Instrum. Methods* 156 (3) (1978) 459–476, [http://dx.doi.org/10.1016/0029-554X\(78\)90746-2](http://dx.doi.org/10.1016/0029-554X(78)90746-2), URL <http://www.sciencedirect.com/science/article/pii/0029554X78907462>.
- [7] T. Alexander, F. Goulding, An amplitude-insensitive system that distinguishes pulses of different shapes, *Nucl. Instrum. Methods* 13 (1961) 244–246, [http://dx.doi.org/10.1016/0029-554X\(61\)90198-7](http://dx.doi.org/10.1016/0029-554X(61)90198-7), URL <http://www.sciencedirect.com/science/article/pii/0029554X61901987>.
- [8] M. Roush, M. Wilson, W. Hornyak, Pulse shape discrimination, *Nucl. Instrum. Methods* 31 (1) (1964) 112–124, [http://dx.doi.org/10.1016/0029-554X\(64\)90333-7](http://dx.doi.org/10.1016/0029-554X(64)90333-7), URL <http://www.sciencedirect.com/science/article/pii/0029554X64903337>.
- [9] G. Liu, M. Aspinall, X. Ma, M. Joyce, An investigation of the digital discrimination of neutrons and γ rays with organic scintillation detectors using an artificial neural network, *Nucl. Instrum. Methods Phys. Res. A* 607 (3) (2009) 620–628, <http://dx.doi.org/10.1016/j.nima.2009.06.027>, URL <http://www.sciencedirect.com/science/article/pii/S0168900209011966>.
- [10] X. Luo, Y. Wang, J. Yang, G. Liu, C. Lin, Q. Hu, J. Peng, Neutron/gamma discrimination employing the power spectrum analysis of the signal from the liquid scintillator BC501A, *Nucl. Instrum. Methods Phys. Res. A* 717 (2013) 44–50, <http://dx.doi.org/10.1016/j.nima.2013.04.004>, URL <http://www.sciencedirect.com/science/article/pii/S0168900213003835>.
- [11] E. Ronchi, P.-A. Söderström, J. Nyberg, E.A. Sundén, S. Conroy, G. Ericsson, C. Hellesen, M.G. Johnson, M. Weiszflog, An artificial neural network based neutron–gamma discrimination and pile-up rejection framework for the BC-501 liquid scintillation detector, *Nucl. Instrum. Methods Phys. Res. A* 610 (2) (2009) 534–539, <http://dx.doi.org/10.1016/j.nima.2009.08.064>, URL <http://www.sciencedirect.com/science/article/pii/S0168900209017045>.
- [12] P.-A. Söderström, G. Jaworski, J.V. Dobón, J. Nyberg, J. Agramunt, G. de Angelis, S. Carturan, J. Egea, M. Erduran, S. Ertürk, G. de France, A. Gadea, A. Goasduff, V. González, K. Hadyńska-Klek, T. Hüyük, V. Modamio, M. Moszynski, A.D. Nitto, M. Palacz, N. Pietralla, E. Sanchis, D. Testov, A. Triossi, R. Wadsworth, Neutron detection and γ -ray suppression using artificial neural networks with the liquid scintillators BC-501A and BC-537, *Nucl. Instrum. Methods Phys. Res. A* 916 (2019) 238–245, <http://dx.doi.org/10.1016/j.nima.2018.11.122>, URL <http://www.sciencedirect.com/science/article/pii/S0168900218317753>.
- [13] E. Doucet, T. Brown, P. Chowdhury, C. Lister, C. Morse, P. Bender, A. Rogers, Machine learning n/? discrimination in CLYC scintillators, *Nucl. Instrum. Methods Phys. Res. A* (2018) <http://dx.doi.org/10.1016/j.nima.2018.09.036>, URL <http://www.sciencedirect.com/science/article/pii/S016890021831180X>.
- [14] A. Gadea, E. Farnea, J. Valiente-Dobón, B. Million, D. Mengoni, D. Bazzacco, F. Recchia, A. Dewald, T. Pissulla, W. Rother, G. de Angelis, A. Austin, S. Aydin, S. Badoer, M. Bellato, G. Benzoni, L. Berti, R. Beunard, B. Birkenbach, E. Bissiat, N. Blasi, C. Boiano, D. Bortolato, A. Bracco, S. Brambilla, B. Bruyneel, E. Calore, F. Camera, A. Capsoni, J. Chavas, P. Cocconi, S. Coelli, A. Colombo, D. Conventi, L. Costa, L. Corradi, A. Corsi, A. Cortesi, F. Crespi, N. Dosme, J. Eberth, S. Fantinel, C. Fanin, E. Fioretto, C. Fransen, A. Giaz, A. Gottardo, X. Grave, J. Grebosz, R. Griffiths, E. Grodner, M. Gulmini, T. Habermann, C. He, H. Hess, R. Isocrate, J. Jolie, P. Jones, A. Latina, E. Legay, S. Lenzi, S. Leoni, F. Lelli, D. Lersich, S. Lunardi, G. Maron, R. Menegazzo, C. Michelagnoli, P. Molini, G. Montagnoli, D. Montanari, O. Möller, D. Napoli, M. Nicoletto, R. Nicolini, M. Ozille, G. Pascovici, R. Peghin, M. Pignanelli, V. Pucknell, A. Pullia, L. Ramina, G. Rampazzo, M. Rebeschini, P. Reiter, S. Riboldi, M. Rigato, C.R.

- Alvarez, D. Rosso, G. Salvato, J. Strachan, E. Sahin, F. Scarlassara, J. Simpson, A. Stefanini, O. Stezowski, F. Tomasi, N. Toniolo, A. Triossi, M. Turcato, C. Ur, V. Vandone, R. Venturelli, F. Veronese, C. Veysière, E. Viscione, O. Wieland, A. Wiens, F. Zocca, A. Zucchiatti, Conceptual design and infrastructure for the installation of the first AGATA sub-array at LNL, Nucl. Instrum. Methods Phys. Res. A 654 (1) (2011) 88–96, <http://dx.doi.org/10.1016/j.nima.2011.06.004>, URL <http://www.sciencedirect.com/science/article/pii/S0168900211011132>.
- [15] D. Ralet, S. Pietri, Y. Aubert, M. Bellato, D. Bortolato, S. Brambilla, F. Camera, N. Dosme, A. Gadea, J. Gerl, P. Golubev, X. Grave, H. Johansson, N. Karkour, A. Korichi, N. Kurz, X. Lafay, E. Legay, D. Linget, N. Pietralla, D. Rudolph, H. Schaffner, O. Stezowski, B. Travers, O. Wieland, Data-flow coupling and data-acquisition triggers for the PreSPEC-AGATA campaign at GSI, Nucl. Instrum. Methods Phys. Res. A 786 (2015) 32–39, <http://dx.doi.org/10.1016/j.nima.2015.03.025>, URL <http://www.sciencedirect.com/science/article/pii/S0168900215003332>.
- [16] E. Clément, C. Michelagnoli, G. de France, H. Li, A. Lemasson, C.B. Dejean, M. Beuzard, P. Bougault, J. Caccitti, J.-L. Foucher, G. Fremont, P. Gangnant, J. Goupil, C. Houarner, M. Jean, A. Lefevre, L. Legeard, F. Legruel, C. Maugeais, L. Ménager, N. Ménard, H. Munoz, M. Ozille, B. Raine, J. Ropert, F. Saillant, C. Spitaels, M. Tripon, P. Vallerand, G. Voltolini, W. Korten, M.-D. Salsac, C. Theisen, M. Zielińska, T. Joannem, M. Karolak, M. Kebbiri, A. Lotode, R. Touzery, C. Walter, A. Korichi, J. Ljungvall, A. Lopez-Martens, D. Ralet, N. Dosme, X. Grave, N. Karkour, X. Lafay, E. Legay, I. Kojouharov, C. Domingo-Pardo, A. Gadea, R. Pérez-Vidal, J. Civera, B. Birkenbach, J. Eberth, H. Hess, L. Lewandowski, P. Reiter, A. Nannini, G.D. Angelis, G. Jaworski, P. John, D. Napoli, J. Valiente-Dobón, D. Barrientos, D. Bortolato, G. Benzoni, A. Bracco, S. Brambilla, F. Camera, F. Crespi, S. Leoni, B. Million, A. Pullia, O. Wieland, D. Bazzacco, S. Lenzi, S. Lunardi, R. Menegazzo, D. Mengoni, F. Recchia, M. Bellato, R. Isocrate, F.E. Canet, F. Didierjean, G. Duchêne, R. Baumann, M. Brucker, E. Dangelser, M. Filliger, H. Friedmann, G. Gaudiot, J.-N. Grapton, H. Kocher, C. Mathieu, M.-H. Sigward, D. Thomas, S. Veeramootoo, J. Dudouet, O. Stézowski, C. Aufranc, Y. Aubert, M. Labiche, J. Simpson, I. Burrows, P. Coleman-Smith, A. Grant, I. Lazarus, P. Morrall, V. Pucknell, A. Boston, D. Judson, N. Lalović, J. Nyberg, J. Collado, V. González, I. Kuti, B. Nyakó, A. Maj, M. Rudigier, Conceptual design of the AGATA 1π array at GANIL, Nucl. Instrum. Methods Phys. Res. A 855 (2017) 1–12, <http://dx.doi.org/10.1016/j.nima.2017.02.063>, URL <http://www.sciencedirect.com/science/article/pii/S0168900217302590>.
- [17] Ö. Skeppstedt, H. Roth, L. Lindström, R. Wadsworth, I. Hibbert, N. Kelsall, D. Jenkins, H. Grawe, M. Górski, M. Moszyński, Z. Sujkowski, D. Wolski, M. Kapusta, M. Hellström, S. Kalogeropoulos, D. Oner, A. Johnson, J. Cederkäll, W. Klamra, J. Nyberg, M. Weiszflog, J. Kay, R. Griffiths, J.G. Narro, C. Pearson, J. Eberth, The EUROBALL neutron wall – design and performance tests of neutron detectors, Nucl. Instrum. Methods Phys. Res. A 421 (3) (1999) 531–541, [http://dx.doi.org/10.1016/S0168-9002\(98\)01208-X](http://dx.doi.org/10.1016/S0168-9002(98)01208-X), URL <http://www.sciencedirect.com/science/article/pii/S016890029801208X>.
- [18] J. Ljungvall, M. Palacz, J. Nyberg, Monte Carlo simulations of the Neutron Wall detector system, Nucl. Instrum. Methods Phys. Res. A 528 (3) (2004) 741–762, <http://dx.doi.org/10.1016/j.nima.2004.05.032>, URL <http://www.sciencedirect.com/science/article/pii/S016890020400988X>.
- [19] J. Scheurer, M. Aiche, M. Aleonard, G. Barreau, F. Bourguine, D. Boivin, D. Cabaussel, J. Chemin, T. Doan, J. Goudour, M. Harston, A. Brondi, G.L. Rana, R. Moro, E. Vardaci, D. Curien, Improvements in the in-beam γ -ray spectroscopy provided by an ancillary detector coupled to a Ge γ -spectrometer: the DIAMANT-EUROGAM II example, Nucl. Instrum. Methods Phys. Res. A 385 (3) (1997) 501–510, [http://dx.doi.org/10.1016/S0168-9002\(96\)01038-8](http://dx.doi.org/10.1016/S0168-9002(96)01038-8), URL <http://www.sciencedirect.com/science/article/pii/S0168900296010388>.
- [20] G. Jaworski, A. Goasduff, F.E. Canet, V. Modamio, T. Huyuk, A. Triossi, M. Jastrzab, Söderström, S. Carturan, A.D. Nitto, G. de Angelis, G.D. France, N. Erduran, A. Gadea, M. Moszynski, J. Nyberg, M. Palacz, J. Valiente, R. Wadsworth, R. Aliaga, C. Aufranc, M. Bezdard, G. Beaulieu, P. Bednarczyk, E. Bisiato, A. Boujrad, I. Burrows, E. Clement, P. Cocconi, G. Colucci, D. Conventi, M. Cordwell, S. Coudert, J. Deltoro, L. Ducroux, T. Dupasquier, S. Ertürk, X. Fabian, V. González, A. Gottardo, A. Grant, K. Hadyńska-Klek, A. Illana, M. Jurado-Gomez, M. Kogimtzis, I. Lazarus, L. Legeard, J. Ljungvall, A. Maj, G. Pasqualato, R. Perez-Vidal, A. Raggio, D. Ralet, N. Redon, F. Saillant, E. Sanchis, B. Saygı, M. Scarciollo, M. Siciliano, O. Stezowski, D. Testov, M. Tripon, I. Zanon, The new neutron multiplicity filter NEDA and its first physics campaign with AGATA, Acta Phys. Polon. B 50 (3) (2019) 585, <http://dx.doi.org/10.5506/APhysPolB.50.585>.
- [21] F.J.E. Canet, V. González, M. Tripon, M. Jastrzab, A. Triossi, A. Gadea, G. de France, J.J. Valiente-Dobón, D. Barrientos, E. Sanchis, A. Boujrad, C. Houarner, M. Blaizot, P. Bourgault, G. de Angelis, M.N. Erduran, S. Ertürk, T. Hüyük, G. Jaworski, X.L. Luo, V. Modamio, M. Moszyński, A.D. Nitto, J. Nyberg, P. Söderström, M. Palacz, R. Wadsworth, A new front-end high-resolution sampling board for the new-generation electronics of EXOGAM2 and NEDA detectors, IEEE Trans. Nucl. Sci. 62 (3) (2015) 1056–1062, <http://dx.doi.org/10.1109/TNS.2015.2433021>.
- [22] M. Bellato, D. Bortolato, J. Chavas, R. Isocrate, G. Rampazzo, A. Triossi, D. Bazzacco, D. Mengoni, F. Recchia, Sub-nanosecond clock synchronization and trigger management in the nuclear physics experiment AGATA, J. Instrum. 8 (07) (2013) P07003, <http://dx.doi.org/10.1088/1748-0221/8/07/p07003>.
- [23] S. Hochreiter, J. Schmidhuber, Long short-term memory, Neural Comput. 9 (8) (1997) 1735–1780.
- [24] M. Abadi, A. Agarwal, P. Barham, E. Brevdo, Z. Chen, C. Citro, G.S. Corrado, A. Davis, J. Dean, M. Devin, S. Ghemawat, I. Goodfellow, A. Harp, G. Irving, M. Isard, Y. Jia, R. Jozefowicz, L. Kaiser, M. Kudlur, J. Levenberg, D. Mané, R. Monga, S. Moore, D. Murray, C. Olah, M. Schuster, J. Shlens, B. Steiner, I. Sutskever, K. Talwar, P. Tucker, V. Vanhoucke, V. Vasudevan, F. Viégas, O. Vinyals, P. Warden, M. Wattenberg, M. Wicke, Y. Yu, X. Zheng, TensorFlow: Large-scale machine learning on heterogeneous systems, 2015, URL <http://tensorflow.org/>, Software available from tensorflow.org.
- [25] F. Chollet, et al., Keras, 2015, <https://keras.io>.